

Analysis of the Dissociation of H₂O in Water Using First-Principles Molecular DynamicsBernhardt L. Trout^{*,†} and Michele Parrinello

Max-Planck-Institut für Festkörperforschung, Heisenbergstrasse 1, 70569 Stuttgart, Germany

Received: February 15, 1999; In Final Form: July 6, 1999

We have analyzed the structural, electronic, and dynamic properties along the reaction path of the dissociation of an H₂O molecule in bulk water. There are four stages to the dissociation process, the last step being effected by a separation of hydroxyl and hydronium ions by two solvation shells. Structural as well as electronic data bear out this interpretation. In addition, by analyzing the electron localization function (ELF) around the oxygen in the hydroxyl ion, the question of why this species is most often 4-fold coordinated is addressed. The explanation arising from ELF is that unpaired electrons are symmetrically localized in a ring-shape around the O atom leading to the possibility of a planar solvation shell as observed in *ab initio* simulations. Finally, a dynamic analysis gives an indication of the femtosecond time-scale of the solvent response.

1. Introduction

Water is perhaps the most important compound in chemistry, playing an essential role in biological phenomena, acid–base reactions, electrochemical processes, and industrial chemical production. The details of its chemistry, however, are not well understood because of their extreme complexity. This complexity arises from its bonding structure, its polarizability, and the range of time scales of processes associated with it. The latter covers 18 orders of magnitude ranging from femtoseconds for some relaxation processes to hours for the dissociation of an H₂O molecule.^{1–12}

In order to study such processes theoretically, techniques must be used which accurately treat the electronic degrees of freedom and in particular, bond breaking and bond formation. First-principles molecular dynamics is such a technique, and within the framework of Car–Parrinello,¹³ it has been used successfully to study the structural and electronic properties of simulated water^{14,15} and the solvation and transport of hydronium and hydroxyl ions in water.¹⁶ As reported in a recent Letter, we have used the results of Car–Parrinello simulations to propose a mechanism for the dissociation process of H₂O in water:¹⁷



In this study, we use the results of these simulations to analyze the structural and electronic changes that occur in water on the route to dissociation in addition to the femtosecond and picosecond time-scale processes along the route.

2. Methodology

The Car–Parrinello method combines a quantum mechanical treatment of the electrons via density functional theory¹⁸ and a classical treatment of the nuclei, which are moved via a molecular dynamics simulation. Because the specific methodology used in ref 15 best reproduced experimental results on bulk water, we have used it in our study. In particular, we have used the BLYP^{19,20} functional, Martins–Troullier pseudopotentials²¹ with a plane-wave cutoff of 70 Ry and a model of 32 water

molecules in a cubic box with periodic boundary conditions. In order to determine properties averaged within the canonical ensemble, a Nosé–Hoover chain thermostat with a length of 4 and a characteristic frequency of 500 cm^{−1} was used on the nuclear degrees of freedom.^{22–25} (*vide infra* for a discussion on the possible effects of the choice of frequency.) Each run lasted 2 ps. During the first picosecond, the system was relaxed, and during the second, accumulated data was averaged to determine properties of interest. One picosecond of averaging was found to be enough to calculate the properties reported in this paper with small statistical uncertainties. Nevertheless, because of the short time of the simulations, there will be statistical uncertainties associated with other properties of the system. To ascertain the magnitude of these uncertainties, one would need to perform much longer simulations. Note that for the reasons described in ref 15, D is substituted for H in the simulation. Therefore, in the discussion below, it should be kept in mind that all species designated “H” are D species. Further methodological details can be found in references and in the subsections below.

3. Results and Discussion

3.1. Thermodynamics of Dissociation. The dissociation of H₂O is a slow event, occurring on the time scale of about 11 h per molecule.² This time scale is clearly outside of the scope of a normal molecular dynamics simulation, so in order to study the process, we have chosen a reaction coordinate, and constrained its value over a range large enough to effect dissociation. In particular, we have chosen as the reaction coordinate the H–O distance of an arbitrarily picked water molecule, and constrained its value between 1.1 and 1.8 Å, with 0.1 Å increments. This particular choice of the reaction coordinate allowed the system to evolve during the simulation with as much freedom as possible. Note that data presented below for the unconstrained system is included in the graphs at the point where the value of the constraint equals 1.0 Å, the average O–H bond distance in liquid water. The H atom and the O atom which are constrained are labeled H* and O*, respectively, the O atom which neighbors H* is labeled O', and the reaction coordinate is labeled $r_{\text{O}^*\text{H}^*}$, where $r_{\text{O}^*\text{H}^*} = |\mathbf{r}_{\text{O}^*} - \mathbf{r}_{\text{H}^*}|$.

At each point along the reaction coordinate, the ensemble-averaged force due to the constraint along the constrained

[†] Current address: Department of Chemical Engineering, Massachusetts Institute of Technology, 77 Massachusetts Avenue, Room 66-556, Cambridge, MA 02139.

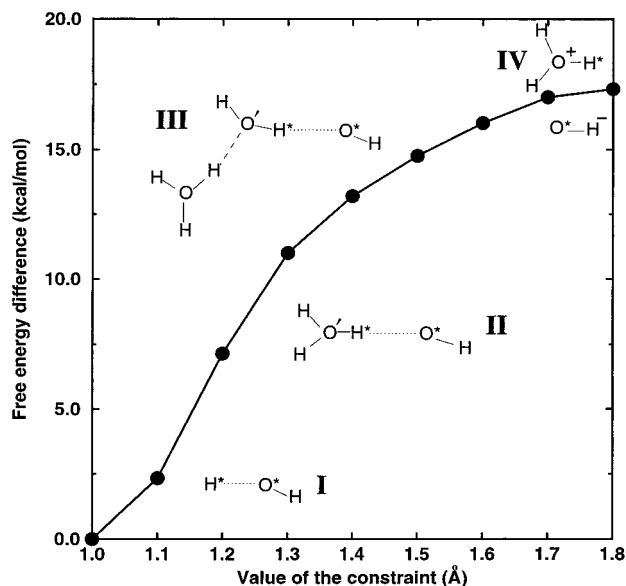


Figure 1. Free energy profile along the reaction coordinate. The dotted lines in the schematics represent the constraint, and the dashed line a hydrogen bond.

direction was evaluated. (Note that this force is equivalent to the Lagrange undetermined multiplier found by solving the equations of motion of the system with the imposed constraint.) This force can be related to the change in the free energy by the following formula:²⁶

$$\frac{dF}{dr_{O^*H^*}} = \frac{\langle Z^{-1/2}[-f + kTG] \rangle_{r_{O^*H^*}}}{\langle Z^{-1/2} \rangle_{r_{O^*H^*}}} \quad (2)$$

where F is the free energy, $r_{O^*H^*}$ is the length of the constraint (fixed during a given simulation), f is the force due to the constraint along the constrained direction, and Z and G are mass-weighted factors associated with the transformation from generalized to Cartesian coordinates. Details about Z and G can be found in the reference. Because the constraint used in this study is a simple distance constraint, eq 2 reduces to the following form

$$\frac{dF}{dr_{O^*H^*}} = -\langle f \rangle_{r_{O^*H^*}} \quad (3)$$

(Note that eq 3 would also arise from using the blue moon ensemble method²⁷ for our simple constraint.) Thus, the average force on the constraint can be used to determine the free energy as a function of the reaction coordinate by integrating the average force along the reaction coordinate. The free energy curve for H₂O dissociation is presented in Figure 1. For this study, it is important to note the four stages of dissociation, each of which is depicted at the appropriate points along the free energy curve. (I) Initially, the constrained H*—O* bond is being stretched, and the water molecule is still an intact species. (II) The H* and the O* have been separated to the extent that hydronium and hydroxyl ions have been formed and kept stable by the constraint. (III) The hydronium ion is free to jump between the O' atom adjacent to the H* and the two nearest-neighbor nonconstrained O atoms. (IV) The hydronium and hydroxyl ions become free species. Stage IV occurs when the value of the reaction coordinate is between 1.7 and 1.8 Å. Additional details on the free energy curve and comparison with experiment can be found in ref 17.

3.2. Structural Properties. In order to gain additional insight into the dissociation process, we have analyzed ensemble

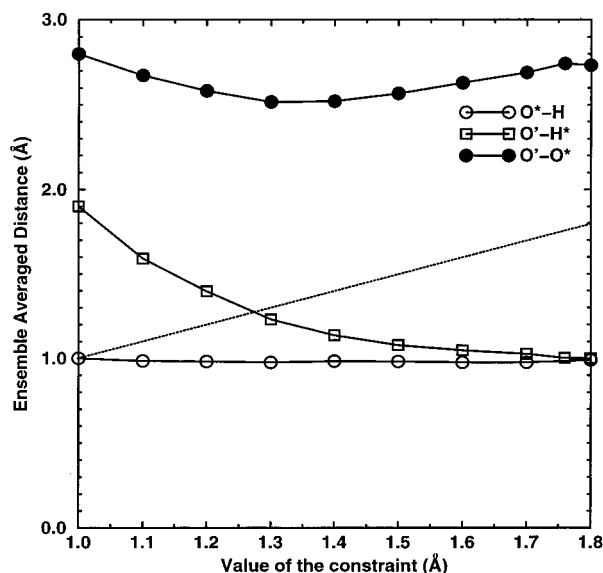


Figure 2. Selected average bond distances as a function of reaction coordinate. The dotted line is the curve $y = x$.

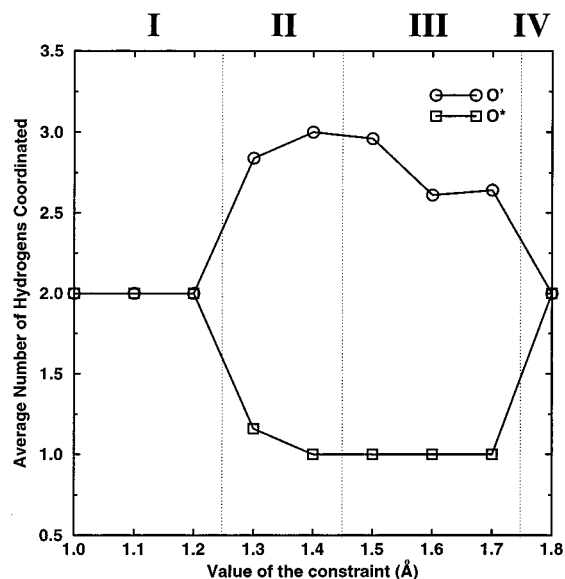


Figure 3. Average hydrogen coordination number on O* and O'.

averaged structural properties. Figure 2 depicts the average O'—H* and O'—O* distances as a function of reaction coordinate. Focusing on the O' and H* distances, we can see that when there is no constraint (the point on the graph where the value of the abscissa is 1.0 Å, the average O—H distance in an H₂O molecule), the O'—H* distance is that of a hydrogen bond. As the constraint is imposed and its value is increased, the O'—H* distance smoothly decreases until it reaches the value of the average O—H distance in an H₂O molecule. The dotted line is the curve $y = x$. At the point at which it intersects the O'—H* curve, the value of the constraint is equal to the average O'—H* distance. This point occurs at just under $r_{O^*H^*} = 1.3$ Å, signifying that for $r_{O^*H^*} \geq 1.3$ Å, the transition to stage II has occurred. This conclusion is reinforced by the curve of the O'—O* distance as a function of reaction coordinate. Here, the minimum occurs at $r_{O^*H^*} = 1.3$ Å, implying that this is the point at which the H* transfers from the O* to the O'.

Figure 3 presents the average hydrogen coordination number of O' and of O* as a function of reaction coordinate. This hydrogen coordination number is found for each time step along

the trajectory by (1) assigning each H atom to its nearest O atom (this procedure uniquely associates one O atom with each H atom) and (2) adding up the number of H atoms uniquely assigned to each O atom. The hydrogen coordination number is then averaged along each trajectory. This information can be used as a measure of how similar the environment of an O atom is to the environments of the O atoms in OH^- , H_2O , and H_3O^+ . These species have coordination numbers of 1.0, 2.0, and 3.0, respectively. Starting from $r_{\text{O}^*\text{H}^*} = 1.0 \text{ \AA}$ and going to $r_{\text{O}^*\text{H}^*} = 1.2 \text{ \AA}$, both O' and O^* have an average coordination number of 2.0, implying that they are in a similar environment to the O atom in H_2O . When $r_{\text{O}^*\text{H}^*} = 1.3 \text{ \AA}$, the average coordination numbers of O' and O^* become 2.84 and 1.16, respectively, demonstrating that the O' and O^* are essentially in environments similar to H_3O^+ and OH^- respectively, with fluctuations from perfect H_3O^+ and OH^- species. At $r_{\text{O}^*\text{H}^*} = 1.4 \text{ \AA}$, the average coordination numbers of O' and O^* are 3.0 and 1.0, so that they have become H_3O^+ and OH^- species held apart by the constraint.

From $r_{\text{O}^*\text{H}^*} = 1.4 \text{ \AA}$ up until $r_{\text{O}^*\text{H}^*} = 1.8 \text{ \AA}$, the point at which the hydronium and hydroxyl ions become free species, the average coordination number of O^* is 1.0, showing that it remains essentially an OH^- species. The average coordination number of the O' atom, however, begins to decrease gradually at $r_{\text{O}^*\text{H}^*} = 1.5 \text{ \AA}$ and does not reach the value of 2.0 until $r_{\text{O}^*\text{H}^*} \sim 1.8 \text{ \AA}$. At this stage, the hydronium ion is hopping between the O' atom and the two nonconstrained O atoms adjacent to the O' atom. At $r_{\text{O}^*\text{H}^*} = 1.8 \text{ \AA}$, the average coordination number of both O' and O^* becomes 2.0, and the two atoms are essentially in a similar environment to the O atom in H_2O . This is because the hydronium and hydroxyl ions have begun to structurally diffuse away, which leads to the reconvergence of the two curves in Figure 3. In summary, stages of dissociation as depicted in Figure 1 can be related to the value of the constraint as follows: (I) $r_{\text{O}^*\text{H}^*} = 1.0\text{--}1.2 \text{ \AA}$, (II) $r_{\text{O}^*\text{H}^*} = 1.3\text{--}1.4 \text{ \AA}$, (III) $r_{\text{O}^*\text{H}^*} = 1.5\text{--}1.7 \text{ \AA}$, and (IV) $r_{\text{O}^*\text{H}^*} \geq 1.8 \text{ \AA}$.

3.3. Measures of Bonding and Charge Transfer. First-principle methods, such as density functional theory, provide a unique advantage in that the electronic structure is calculated and thus can be analyzed to gain direct insight into bonding and charge transfer. This section focuses on electron populations, atomic charges and electron localization in order to elucidate the changes in the electronic state of the system during the dissociation process. Configurations have been selected at random from the equilibrated part of the trajectory for no constraint and for values of $r_{\text{O}^*\text{H}^*} = 1.1\text{--}1.4 \text{ \AA}$. The same has been done for $r_{\text{O}^*\text{H}^*} = 1.8 \text{ \AA}$, except the configuration chosen was slightly before equilibration (*vide infra*). Remember that for $r_{\text{O}^*\text{H}^*} = 1.1\text{--}1.4 \text{ \AA}$, the hydronium ion has not yet begun to hop, and the configurations considered are either an H_2O molecule with a stretched bond or a hydronium and a hydroxyl ion that are held apart by the constraint. For $r_{\text{O}^*\text{H}^*} = 1.8 \text{ \AA}$, a configuration was chosen in which the O^* is in a hydroxyl ion, before it begins to hop. The configuration chosen is very much like the one for stage III as depicted in Figure 1.

In Figure 4, the Mulliken populations²⁸ of H^* , O' , and O^* are presented as a function of the reaction coordinate. In addition, in Figure 5, the charges of these atoms, as determined by the method of Hirshfeld,²⁹ are presented. It should be emphasized that any method of dividing the electronic structure of a condensed system (and also of a molecule) has an element of arbitrariness.

Most immediately evident is that none except for one of the six curves is monotonic for the first five points. One might

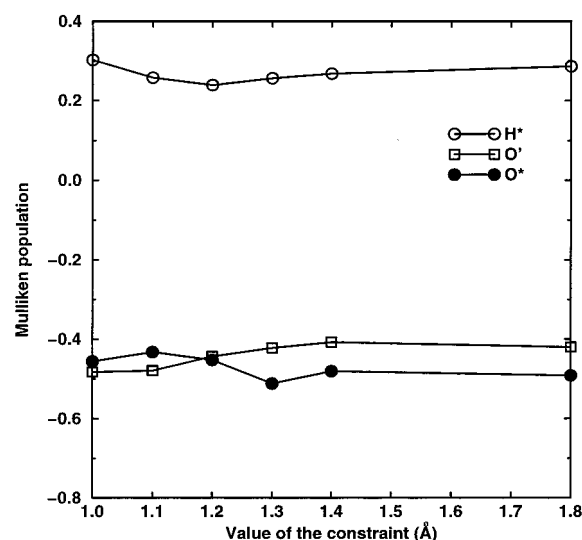


Figure 4. Mulliken populations as a function of reaction coordinate for H^* , O^* , and on O' .

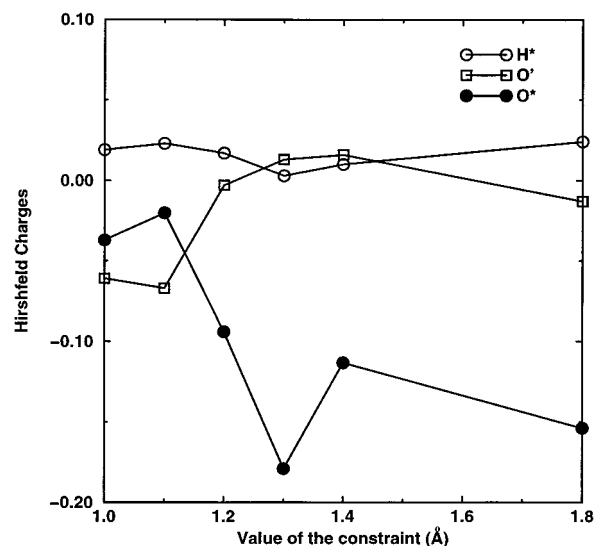


Figure 5. Hirshfeld charges as a function of reaction coordinate for H^* , O^* , and on O' .

expect that as the value of the constraint is increased toward $r_{\text{O}^*\text{H}^*} = 1.4 \text{ \AA}$, the charge on H^* would become more positive (electron population decreasing), the charge on O' would become more positive (electron population decreasing), and the charge on O^* would become more negative (the electron population increasing). In fact, the rough trends are this way, but there are various minima and maxima, which are not even consistent between the Mulliken population analysis and the Hirshfeld charge analysis. This is a reflection of the limitations of both methods of charge analysis, and at this stage, we can attribute a physical reasoning only to the general trends and not to the details.

Another way of analyzing bonding and charge is by calculating the electron localization function (ELF). This function, which depends on spatial position, was recently proposed by Becke and Edgecombe³⁰ and has had several successful applications.^{31–34} ELF is an inverse function of the parameter χ :

$$\text{ELF} = \frac{1}{(1 + \chi)^2} \quad (4)$$

where

$$\chi = \frac{\sum_i |\psi_i|^2 - \frac{1}{4} \frac{(\nabla \rho)^2}{\rho}}{C \rho^{5/3}} \quad (5)$$

Thus, χ is the difference between the electronic kinetic energy with Pauli exclusion and the electronic kinetic energy without Pauli exclusion normalized to the electronic kinetic energy of a homogeneous electron gas.³¹ ELF is an inverse function of χ , chosen so that its value is between 0 and 1, where 1 indicates that the electron is most localized.

Isosurfaces of ELF can be calculated and used to help explain the bonding structure and charge localization in a chemical system. Very recently, it has been shown that the topological properties of the ELF can be used to understand otherwise elusive bonding structures.³⁵ In Figure 6, we show the ELF isosurface in the gas phase and in the liquid. Figures 6a and 6b exhibit the presence of the lone pairs of electrons on the O atom in the form of a banana-shaped surface. This surface is reducible at higher values of the ELF and splits into two tear drop shaped surfaces as shown in Figure 6c. In Figures 6, b and c, it is evident that the topological structure is preserved and only slightly distorted in the liquid state. Furthermore, the lone pairs of electrons in the system play a crucial role in establishing the H-bond.

Similarly, the analysis of the ELF isosurfaces for the OH⁻ and H₃O⁺ in the gas phase, shown in Figure 7, is an important prerequisite for understanding the ELF isosurfaces of these ions in water. The isosurface around the H atom in OH⁻ looks qualitatively similar to those around the H atoms in bulk water. The major difference is in the isosurface around the O atom. This surface has the shape of a halo (deviations from perfect symmetry are due to sampling with a finite grid), which is irreducible, meaning that as the value of the isosurface is increased, the halo does not break into multiple domains. The isosurfaces around the H atoms in the gas-phase H₃O⁺ are also similar to those around the H atoms in bulk water. There is, however, a qualitatively different domain resulting from the nonbonding pair of electrons. This domain is in the shape of a compressed sphere and is located below the O atom so that a line from the plane formed by the three points of the H nuclei going through the O nucleus intersects the center of the compressed sphere. In contrast with the related surface in the case of H₂O, this surface is irreducible. These shapes, which differ from the shapes of the isosurfaces associated with H₂O molecules, have consequences for the dissociation process and the structure of bulk water (*vide infra*).

Figure 8 shows how the ELF evolves during the dissociation process. As the value of the constraint is increased, it goes from having a distorted water-like shape to one similar to that of the gas phase species OH⁻ and H₃O⁺. One can recognize the OH⁻ halo distorted by the disorder of the liquid (top of Figure 8d) and distorted shape of the H₃O⁺ surface (bottom of Figure 8c and bottom right of Figure 8d).

This topological analysis of the ELF around the hydroxyl ion helps explain the coordination of the hydroxyl ion in water, previously reported by Tuckerman et al.¹⁶ Tuckerman et al., having performed Car–Parrinello simulations of a hydroxyl ion in water, showed that the O atom in the hydroxyl ion has a predominately planar 4-fold coordination. It might be expected, however, to have a tetrahedral 3-fold coordination, since this structure would fit more naturally within the hydrogen bonding network of water. Tuckerman et al. did in fact observe this tetrahedral 3-fold coordination occasionally and showed that it is necessary for proton transfer to occur. Nevertheless, they

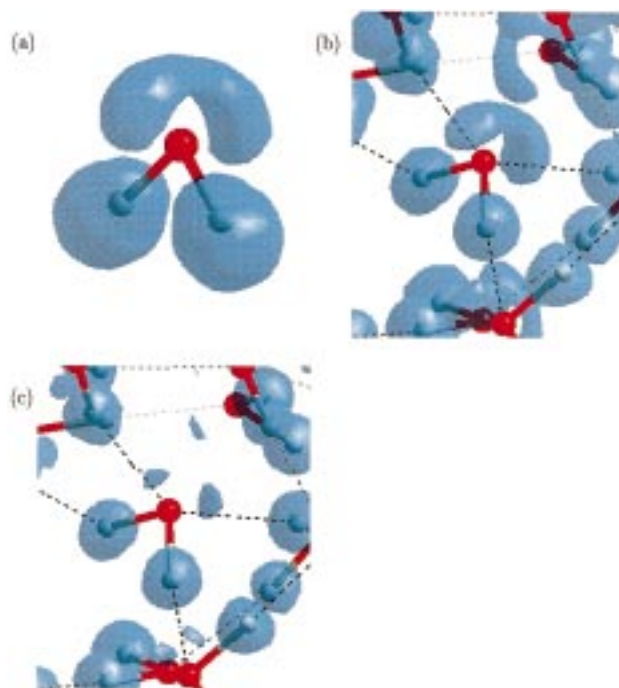


Figure 6. ELF isosurfaces for gas phase H₂O and for H₂O in bulk water: (a) gas phase H₂O, ELF = 0.87; (b) H₂O in bulk water, ELF = 0.87; (c) H₂O in bulk water, ELF = 0.90.

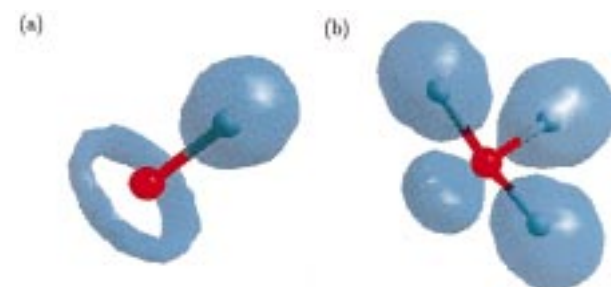


Figure 7. ELF isosurfaces for gas phase OH⁻ and H₃O⁺: (a) gas phase OH⁻, ELF = 0.87; (b) gas phase H₃O⁺, ELF = 0.87.

found that the planar 4-fold coordination is predominant. Note that Novoa et al.³⁶ found that the planar 4-fold coordinated structure to be most stable for large gas phase clusters of a hydroxyl ion solvated by water molecules.

The ELF halo structure around the hydroxyl ion shows that the localization of the electrons (and thus the charge) is symmetric on average. Thus, there are no preferred directions for the hydrogen bonding around the O atom of the hydroxyl ion in the plane of the electron localization. The 4-fold coordination is thus the most favorable tradeoff between the distortion of the hydrogen-bonding network of the H₂O molecules and the energetically favorable hydrogen-bonding interaction between the H₂O molecules and the OH⁻ ion. For the hydronium ion, the localized negative charge in the compressed sphere structure under the O atom also presents the possibilities for hydrogen bonding, as shown in Figure 8c.

3.4. Ultrafast Relaxation Processes. Up to this point, the discussion has been based on the results of Car–Parrinello molecular dynamics simulations used to calculate time-independent properties. A major advantage of molecular dynamics simulations, however, is that dynamic information can be obtained. In this section, we discuss our dynamic results and their implications for solvent relaxation, the dissociation process and dynamic friction.

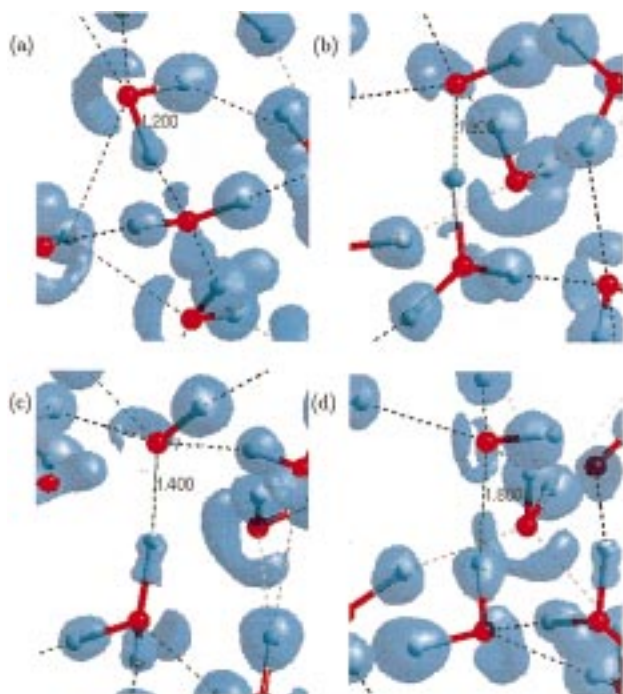


Figure 8. ELF isosurfaces for the region around the constraint at various values of the reaction coordinate. All isosurfaces are at $\text{ELF} = 0.87$. (a) $r_{\text{O}^*\text{H}^*} = 1.2 \text{ \AA}$, (b) $r_{\text{O}^*\text{H}^*} = 1.3 \text{ \AA}$, (c) $r_{\text{O}^*\text{H}^*} = 1.4 \text{ \AA}$, and (d) $r_{\text{O}^*\text{H}^*} = 1.8 \text{ \AA}$.

The most direct dynamic information that can be obtained from this particular study is the time autocorrelation function of the average force of constraint, $\zeta(t)$, where

$$\zeta(t) = \langle f(t')f(t'+t) \rangle \quad (6)$$

Such functions, characteristic of dipole–dipole relaxation processes, are presented in Figure 9 for selected values of the constraint. Because of the short simulation times and the fact that only equilibrium information is obtained for a fixed value of the constraint, the results of the time autocorrelation function reported below should be viewed as rough first approximations. Nevertheless, it is clear that the relaxation response of the system is significantly faster for larger values of the constraint. This can be further seen in Figure 10, which presents a characteristic relaxation time as a function of constraint.

We note that our use of the Nosé–Hoover chain thermostat^{22–25} can lead to artificially fast relaxation and a corresponding fast decay of the autocorrelation functions. The characteristic frequency of the thermostat was 500 cm^{-1} , which corresponds to a time period of 67 fs. This should not greatly affect the very fast decays of $\zeta(t)$ occurring when $r_{\text{O}^*\text{H}^*} \geq 1.4 \text{ \AA}$, but could affect the decays presented for $r_{\text{O}^*\text{H}^*} \leq 1.3 \text{ \AA}$. A much more extensive study on relaxation processes in water would be needed to achieve more than our approximate results.

These results do, however, demonstrate that the response of the system depends significantly on the bonding environment directly around a species. It also implies that the environment formed in the first and second solvation shells does not greatly affect the solvent response. We speculate that the difference in the relaxation times is related to the character of the species bonded to the atoms in the constraint. At lower values of the constraint, the constrained bond resembles an OH bond, and thus the bond of the adjacent species to the H^* is a hydrogen bond. At larger values of the constraint, the constrained bond resembles a hydrogen bond, and thus both of the bonds of the

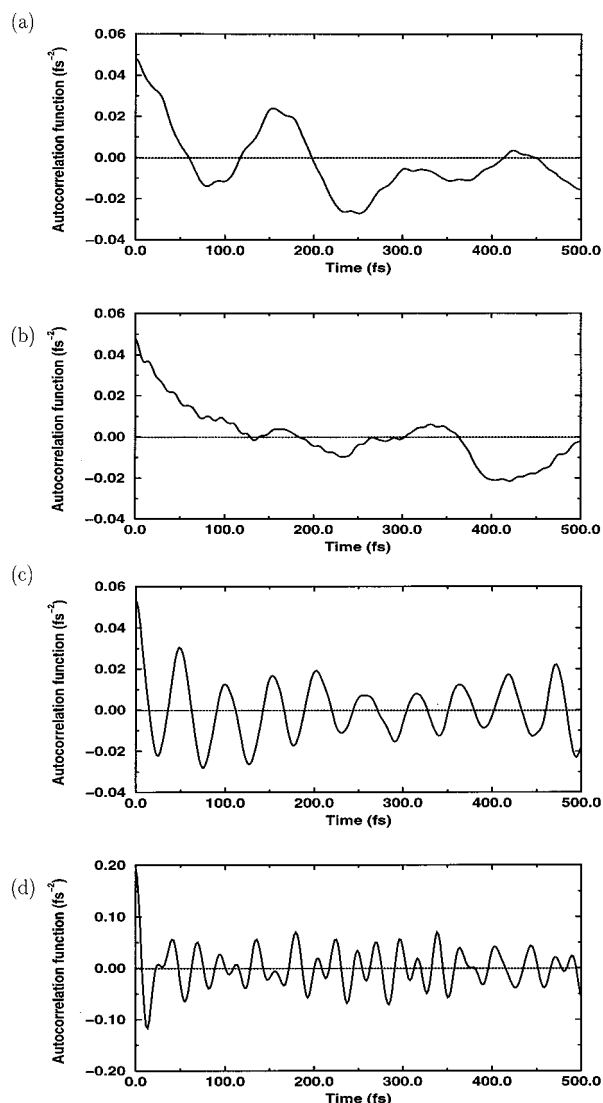


Figure 9. Time autocorrelation functions of the force on the constraint at various values of the reaction coordinate: (a) $r_{\text{O}^*\text{H}^*} = 1.1 \text{ \AA}$, (b) $r_{\text{O}^*\text{H}^*} = 1.2 \text{ \AA}$, (c) $r_{\text{O}^*\text{H}^*} = 1.4 \text{ \AA}$, and (d) $r_{\text{O}^*\text{H}^*} = 1.8 \text{ \AA}$.

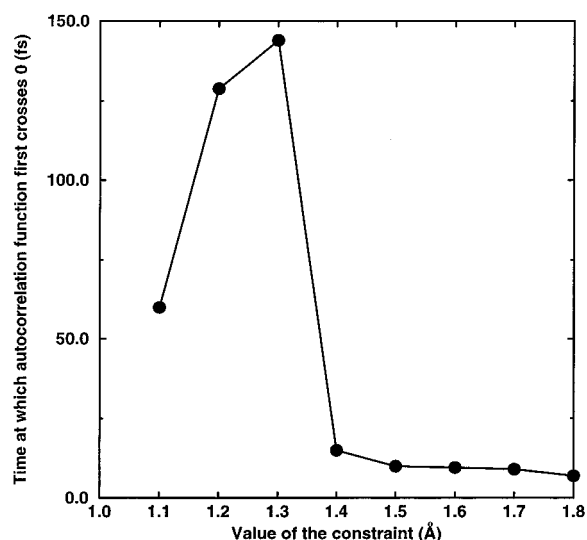


Figure 10. Time of the initial zero point of the autocorrelation function of the force on the constraint as a function of reaction coordinate.

adjacent species to the atoms in the constraint are OH bonds. Since OH bonds should exhibit a faster response than hydrogen

bonds, the autocorrelation function for larger values of the constraint should demonstrate this faster response.

4. Conclusions

We have performed Car–Parrinello molecular dynamics simulations of the dissociation of H₂O in liquid water. We found four different stages in the dissociation process: (I) stretching of an O–H bond in a water molecule, (II) formation of closely associated hydroxyl and hydronium ions, (III) first solvation shell separation of hydroxyl and hydronium ions, and (IV) formation of free products. The different stages can be differentiated via structural, electronic, and dynamic data. An electron localization function (ELF) analysis of the hydroxyl ion adds insight into why its O atom is 4-fold planar coordinated. The nonbonding paired electrons around the O atom in the hydroxyl ion manifest themselves as a symmetric halo (distorted in solution), which would allow planar coordination. The structure of the solvent is such that optimal coordination is 4-fold. Finally, time autocorrelation functions demonstrate that relaxation processes in the solution can occur within femto-second time scales. They reveal differences between solvent relaxation around an O–H bond and solvent relaxation around a hydrogen bond.

Acknowledgment. We thank M. Boero, D. Marx, R. Rousseau, M. Spirk, K.-D. Kreuer, and M. Tuckerman for very helpful discussions.

References and Notes

- (1) Eigen, M. *Z. Phys. Chem.* **1954**, *1*, 176.
- (2) Eigen, M.; Maeyer, L. D. *Z. Elektrochem.* **1955**, *59*, 986.
- (3) Eigen, M. *Angew. Chem.* **1963**, *75*, 489.

- (4) Eigen, M.; Kruse, W.; Maass, G.; Maeyer, L. D. *Prog. React. Kinet.* **1964**, *2*, 285.
- (5) Natzle, W. C.; Moore, C. B. *J. Chem. Phys.* **1985**, *89*, 2506.
- (6) Bader, J. S.; Chandler, D. *Chem. Phys. Lett.* **1989**, *157*, 501.
- (7) Ohmine, I.; Tanaka, H. *Chem. Rev.* **1993**, *93*, 2545.
- (8) Hynes, J. T. *Nature* **1994**, *369*, 439.
- (9) Jimenez, R.; Fleming, G. R.; Kumar, P. V.; Maroncelli, M. *Nature* **1994**, *369*, 471.
- (10) Rossky, P. J.; Simon, J. D. *Nature* **1994**, *370*, 263.
- (11) Stratt, R. M.; Maroncelli, M. *J. Phys. Chem.* **1996**, *100*, 12981.
- (12) Luzar, A.; Chandler, D. *Nature* **1996**, *379*, 55.
- (13) Car, R.; Parrinello, M. *Phys. Rev. Lett.* **1985**, *55*, 2471.
- (14) Laasonen, K.; Sprik, M.; Parrinello, M.; Car, R. *J. Chem. Phys.* **1993**, *99*, 9080.
- (15) Sprik, M.; Hutter, J.; Parrinello, M. *J. Chem. Phys.* **1996**, *105*, 1142.
- (16) Tuckerman, M.; Laasonen, K.; Sprik, M.; Parrinello, M. *J. Chem. Phys.* **1995**, *103*, 150.
- (17) Trout, B. L.; Parrinello, M. *Chem. Phys. Lett.* **1998**, *288*, 343.
- (18) Kohn, W.; Sham, L. J. *Phys. Rev. Lett.* **1965**, *140*, A1133.
- (19) Becke, A. D. *Phys. Rev. A* **1988**, *38*, 3098.
- (20) Lee, C.; Yang, W.; Parr, R. C. *Phys. Rev. B* **1988**, *37*, 785.
- (21) Troullier, N.; Martins, J. *Phys. Rev. B* **1991**, *43*, 1993–2006.
- (22) Nosé, S. *J. Chem. Phys.* **1984**, *81*, 511.
- (23) Nosé, S. *Mol. Phys.* **1984**, *52*, 255.
- (24) Hoover, W. G. *Phys. Rev. A* **1985**, *31*, 1695.
- (25) Martyna, G. J.; Klein, M.; Tuckerman, M. *J. Chem. Phys.* **1992**, *97*, 2635–2643.
- (26) Sprik, M.; Ciccotti, G. *J. Chem. Phys.* **1998**, *109*, 7737–7744.
- (27) Carter, E. A.; Ciccotti, G.; Hynes, J. T.; Kapral, R. *Chem. Phys. Lett.* **1989**, *156*, 472.
- (28) Mulliken, R. S. *J. Chem. Phys.* **1955**, *23*, 1833.
- (29) Hirshfeld, F. L. *Theor. Chim. Acta* **1977**, *44*, 129.
- (30) Becke, A. D.; Edgecomb, K. E. *J. Chem. Phys.* **1990**, *92*, 5397.
- (31) Silvi, B.; Savin, A. *Nature* **1994**, *371*, 683.
- (32) Alikhami, M. E.; Bouteiller, Y.; Silvi, B. *J. Phys. Chem.* **1996**, *100*, 16092.
- (33) Faessler, T. F.; Savin, A. *Chem. Unserer Zeit* **1997**, *31*, 110.
- (34) Savin, A.; Nesper, R.; Wengert, S.; Faessler, T. F. *Angew. Chem., Int. Ed. Engl.* **1997**, *36*, 1808.
- (35) Marx, D.; Savin, A. *Angew. Chem., Int. Ed. Engl.* **1997**, *36*, 2077.
- (36) Novoa, J. J.; Moto, F.; Valle, C. P. d.; Planas, M. *J. Phys. Chem. A* **1997**, *101*, 7842–7853.